Available online at www.sciencedirect.com

ScienceDirect

Procedia CIRP 126 (2024) 543–548

www.elsevier.com/locate/procedia

17th CIRP Conference on Intelligent Computation in Manufacturing Engineering (CIRP ICME '23)

In-source dynamic beam shaping of Al alloys processed via LPBF: effect of novel beam profiles on surface roughness and microstructure

Francesco Galbusera*, Leonardo Caprio, Barbara Previtali, Ali Gökhan Demir

Department of Mechanical Engineering, Politecnico di Milano, Via La Masa 1, I-20156 Milan, Italy

* Corresponding author. *E-mail address:* francesco.galbusera@polimi.it

---

Abstract

Next-generation fiber laser sources can dynamically combine Gaussian beams with ring distributions within the source. The irradiance manipulation may add flexibility to the Laser Powder Bed Fusion process, for instance to control microstructure or surface roughness. However, their use is limited by a lack of studies revealing how beam shaping can be exploited in a reproducible manner. Accordingly, this work shows the use of novel beam profiles provided by a multi-core fiber laser source in the LPBF of AlSi7Mg0.6. Irradiance profiles were characterized, then large experiments were conducted to investigate their effect on surface roughness and microstructure of produced parts.

Peer-review under responsibility of the scientific committee of the 17th CIRP Conference on Intelligent Computation in Manufacturing Engineering (CIRP ICME'23)

Keywords: Beam shaping; Irradiance profile; Non-Gaussian beams; Ring beams; Laser Powder Bed Fusion

---

1. Introduction

The recent development of multi-core high-brilliance fiber laser sources with in-source beam shaping capabilities enabled greater flexibility in the LPBF process. By partitioning the power within the multiple cores of the feeding fiber, these sources allow to manipulate the output laser beam in terms of spatial irradiance distribution. Typically, the beam profiles can be adjusted by selecting predefined power partitions thus allowing to use alternatively conventional Gaussian beams, ring profiles up to doughnut distributions. The introduction of complex beam profiles as alternatives to conventional Gaussian beams could provide better control of the thermal field during the process, thus a precise control of the melt pool shape, the microstructure and mechanical properties [1].

In LPBF, static approaches based on the use of dedicated optical elements have already been addressed to manipulate the irradiance characteristics of the laser beam. Typically, Gaussian beams provided by common fiber laser sources are shaped into non-Gaussian profiles by means of refractive or diffractive lenses. However, these approaches can only provide a fixed phase transformation throughout the process [2]. Despite their limited flexibility, these approaches have demonstrated benefits in LPBF so far, such as greater control of the densification, microstructure properties, surface roughness and tensile properties of AISI316L [1], [3], [4] or an improvement of processing windows of AlSi10Mg [5], [6], IN738LC [7] and CoCrMo [8].

Concerning novel laser sources with beam shaping capabilities, their industrial use was mostly focused on welding applications [9]–[11]. Few works have been published in the LPBF framework demonstrating that the use of ring profiles can increase the processability window of AISI316L [12], [13] and the mechanical properties of AlSi7Mg0.6 [14]. Understanding how the irradiance characteristics of the beam can affect the microstructure properties is fundamental for the reproducible use of non-Gaussian beams in LPBF. In the best of perspectives, manipulating the irradiance profile offers the means to tailor the functional properties of 3D objects. However, systematic investigations on the effect of non-Gaussian beams on microstructure properties and part quality are still missing. Accordingly, the present work studies the effect of novel beam profiles provided by a multi-core fiber laser with in-source

Peer-review under responsibility of the scientific committee of the 17th CIRP Conference on Intelligent Computation in Manufacturing Engineering (CIRP ICME'23)
10.1016/j.procir.2024.08.237

beam shaping capabilities on surface roughness and microstructure properties of a well-known Al-alloy known for its mature LPBF processability, namely AlSi7Mg0.6.

Nomenclature

P	Laser Power (W)
v	Scan speed (mm/s)
h_d	Hatch distance (μm)
z	Layer thickness (μm)
BS	Beam shape index (-)
d_0	Waist diameter (μm)
S_a	Areal surface roughness (μm)
t	Time (ms)

2. Material and methods

2.1. Material

In the present investigation, the aluminum alloy AlSi7Mg0.6 powder produced via gas atomization was used (Carpenter Technology Corporation, Philadelphia, PA, USA). The powder was featured by a spherical morphology with a declared particle size of 20-63 μm.

2.2. LPBF system

The experiments were carried out with an industrial LPBF system (3D-NT LLA150, Torino, Italy). Prior to building, the process chamber was purged and flooded with argon to keep the oxygen content below 0.3 %. A novel fiber laser source with in-source beam shaping capabilities was utilized (nLIGHT AFX 1000, nLIGHT Inc., Vancouver, Washington, USA). The laser source could switch among seven beam profiles, from a conventional Gaussian beam towards a doughnut-like beam, by redistributing the power within a double-core feeding fiber. The beam shapes were indexed sequentially (BSi, with i=0-6) according to the nominal power partitioning declared by the laser source producer [15], [16]. Table 1 resumes the nominal power fractions, the measured diameters according to the $1/e^2$ level in the focal position and the closest Laguerre-Gaussian TEM assignable for each beam profile [17]. The spatial beam profiles acquired at a fixed average laser power of 200 W are depicted in Fig. 1. The beam profiles are displayed in terms of normalized irradiance I/I_{max}, where I_{max} is the peak intensity of the Gaussian beam (index BS0), and radii r.

Table 1: Nominal power ratio of the feeding fiber cores, waist beam diameters d_0 and closest Laguerre-Gaussian TEM representation for each beam shape index BSi.

Beam shape, BS	Power ratio (ring/core)	d_0 (μm)	Closest Laguerre-Gaussian TEM
BS0	0/100	49	TEM$_{00}$
BS1	30/70	50	TEM$_{00}$
BS2	40/60	52	TEM$_{10}$
BS3	50/50	112	TEM$_{10}$
BS4	60/40	128	TEM$_{10}$
BS5	80/20	144	TEM$_{00}$ + TEM$_{01*}$
BS6	90/10	144	TEM$_{01*}$

It should be noted that the Laguerre-Gaussian representation provided in Table 1 are just a rough approximation of the acquired beam shapes since the analytical expressions of the Laguerre-Gaussian modes might be different from the optical acquisitions. Accordingly, when power is concentrated in the central core of the feeding fiber (index BS0-1), the resulting laser beam is a Gaussian-like beam (TEM$_{00}$). Instead, when a rising power is deviated towards the surrounding annulus core (index BS2-4), the resulting beam is approximately a ring-like beam, consisting of a central peak surrounded by a ring (TEM$_{10}$). When power is mostly concentrated in the annulus core of the feeding fiber, the resulting beam resembles a flat-top (index BS5, TEM$_{00}$ + TEM$_{01*}$) or a doughnut distribution (index BS6, TEM$_{01*}$). Consistently, the laser beam diameter in the focus position gradually increases passing from 49 μm for index BS0 up to 144 μm for index BS6.

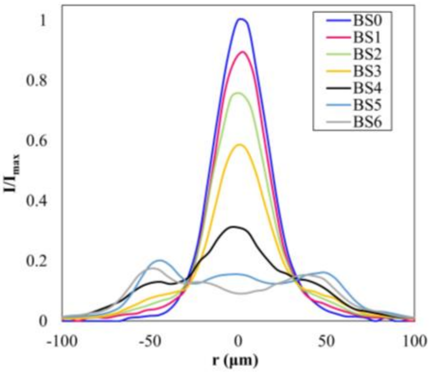

Fig. 1. Spatial beam profiles expressed in terms of I/I_{max} at P = 200 W. Imax is the irradiance peak of the Gaussian distribution (index BS6).

2.3. Experimental plan

Small prismatic samples (5x5x12 mm^3) were produced according to the experimental design shown in Table 2. Laser power (P), scan speed (v) and beam profile (BS) were varied while using a fixed hatch distance (h_d) and layer thickness (z) according to previous experiments. The hatch was scanned with a bidirectional strategy and rotated by 67° each layer.

Table 2: Experimental plan in terms of fixed and varied parameters.

Fixed parameters	
Material	AlSi7Mg0.6
Hatch distance, h_d (μm)	90
Layer thickness, z (μm)	25
Hatch rotation angle, (°)	67
Hatching strategy	Bidirectional
Focal position, (mm)	0
Process gas	Argon
Replicates, n	1
Varied parameters	
Laser power, P (W)	150, 175, 200
Scan speed, v (mm/s)	500, 750, 1000
Beam shape, BS (-)	0, 1, 2, 3, 4, 5, 6

Due to the exploratory nature of the experiment, the conditions were not replicated. The laser source was operated with a Continuous Wave mode and the focal point of the laser beam was set on the powder bed. The samples were built directly on an aluminum alloy baseplate with a similar chemical composition of the powder feedstock.

2.4. Metallographic analysis

Focus variation microscopy was used to acquire the surface topography of the top surfaces using 10X magnification with lateral and vertical resolution of 4 μm and 100 nm respectively (InfiniteFocus, Alicona Imaging GmbH, Graz, Austria) as shown in Fig. 2a. By defining the spatial domain of the acquisition (5x5 mm^2) as illustrated in Fig. 2b, the areal surface roughness (S_a) was furtherly estimated from the microscope control software on the primary profile.

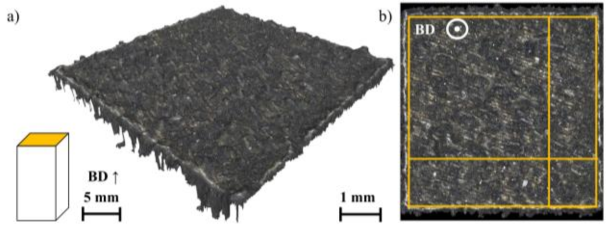

Fig. 2. (a) 3D reconstruction of the sample top surface; (b) Area acquisition for surface areal roughness estimation. BD: Build Direction.

The produced samples were then cut from the substrate with a linear saw and prepared following conventional metallographic procedures. Microstructure was revealed with Keller's reagent (95% H_20, 2.5% HNO_3, 0.3% HCl, 1% HF) [18] and acquired with a Scanning Electron Microscope (Sigma 500 Zeiss FESEM, Oberkochen, Germany). With the same SEM, Electron Back Scattered Diffraction (EBSD) was performed on a restrained batch of samples. The samples were featured by fixed process parameters that guaranteed a densification above 99.5 % (P = 200 W, v = 1000 mm/s) and all the tested beam shapes (BS0-6). These samples were selected to investigate the sole influence of laser beam shape on crystallographic texture and grain structure. The acquisitions were carried out on a cross section parallel to the build direction, with an acquisition field of 180 μm x 140 μm and a spatial resolution of 0.35 μm. Grains were defined by a misorientantion angle larger than 15°, as suggested by Qin et al. [18] dealing with a similar Al-alloy. EBSD data were processed with a dedicated software (AZtec, Oxford Instruments NanoAnalysis, Abingdon, UK).

3. Results and discussion

During the build job a different spatter behaviour could be observed if comparing two equal experimental conditions in terms of scan speed and power but different beam shape. Fig. 3 shows the spatter emission during the processing of the condition with P = 200 W and v = 1000 mm/s, for three representative shapes BS0-3-6. For each sample, some time frames equally spaced of 80 ms were acquired, so as the starting frame from the beginning of laser-material interaction. The frames qualitatively showed that the reduced power in the central core and a rising power over the outer ring produced less spatter.

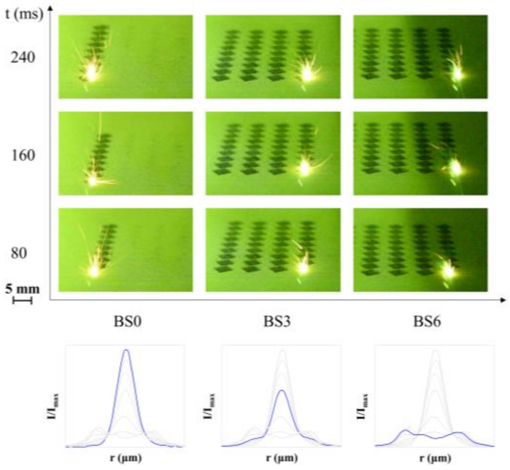

Fig. 3. : Comparison of spatter emission for the condition obtained with P = 200 W, v = 1000 mm/s and BS0-3-6. The values depicted on the y axis refer to the time frames of the acquisition.

3.1. Areal surface roughness

Height maps reconstructed with variable focus microscopy are shown in Fig. 4. The shown conditions refer to all the laser power and beam shapes tested at v = 1000 mm/s. Fig. 4 qualitatively shows the effect of beam shape in the surface roughness reduction. As an instance, at P = 200 W, the surface became smoother and homogenous, especially for the BS6.

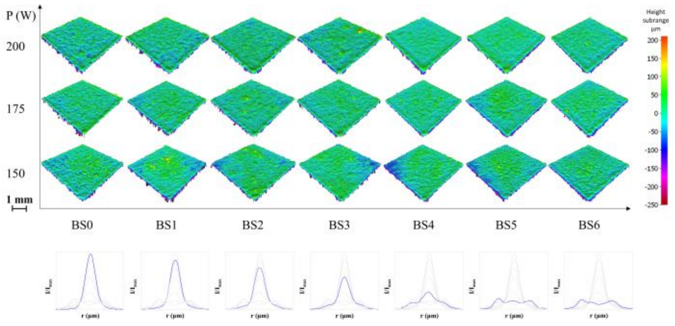

Fig. 4. Height maps of various experimental conditions in terms of laser power (P) and beam shapes (BS) obtained at v = 1000 mm/s. Each surface acquisition has a bounding area of 5x5 mm^2.

This result was also confirmed from the areal surface roughness measurements acquired and shown in Fig. 5 as a function of the process parameters. Moving from a Gaussian beam (index BS0) towards a doughnut distribution (index BS6) appeared to decrease the surface roughness. On the other hand, the effect of scan speed is more difficult to resolve for different BS types. The measurements are coherent with the observation of the spatter generation and densification phenomenon related to the beam intensity [19]. The flatter beams obtained with higher BS showed a reduced surface roughness expected from a more stable melt pool generated via a conduction mode melting process. This result depicts that the surface roughness in the upskin and border regions can be enhanced by the correct allocation of ring beam shapes.

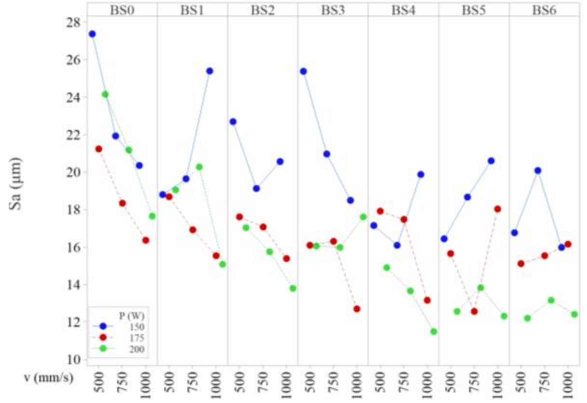

Fig. 5. S_a as a function of the process parameters for each beam shape (BS0-6).

3.2. Microstructure morphology

Microstructure analysis was limited to the samples produced with P = 200 W, v = 1000 mm/s and beam shapes BS0-3-6. This limitation was set to better focus the analysis on the effect of novel beam shapes on microstructure properties rather than the effect of conventional process parameters. Laser power and scan speed levels were chosen as representative conditions of highly dense samples [19].

Fig. 6a-c shows the SEM magnifications of the microstructures after etching. Fig. 6 a1, b1, and c1 display the entire cross section along the build direction. Fig. 6 a2, b2, and c2 show a magnification on a region with several melt pools. Fig. 6 a3, b3, and c3 depict the transition between two melt pools. In Fig. 6 a3), the letter "A", "B" and "C" denote fine, coarse, and heat affected zone (HAZ), respectively. At low magnification, the etched microstructure was made of three different zone across the melt pool: a fine region within the melt pool, a coarse region at the melt pool boundaries and a transition zone identified as the Heat Affected Zone (HAZ). At high magnification, the microstructure morphology shows a cellular/dendritic arrangement ranging from Directional (D) to Non-Directional (ND), which is well known for aluminium hypereutectic alloys [20]. In fact, as described by Qin et al. [18] dealing with AlSi10Mg alloy, the two microstructure morphologies are different views of the same cellular structure. Looking at Fig. 6 b3) and c3), the presence of cellular/dendritic morphology can be confirmed.

Fig. 7 displays additional higher magnifications of the microstructure obtained with BS6. Consistently with literature, at high magnifications microstructure resembles a matrix of α-Aluminium cells in a Si-rich discontinuous network. As observed also in the work of Qin et al. [18], additional Al-Si eutectic lamella are visible. Similar observations can be made for all the tested beam shapes, while crystalline structure and grain sizes requires further investigation through EBSD.

3.3. Grain structure

Fig. 8 shows the orientation maps along build direction, grain size distribution and Inverse Poles and Poles Figures obtained with EBSD on the experimental batch manufactured with P = 200 W, v = 1000 mm/s and all the beam shapes (a-g). As appears from Fig. 8a, when using Gaussian distribution (index BS0), finer grains can be observed in the regions where the mechanism of competitive growth prevails, that is along the melt pool boundaries (depicted with dotted lines).

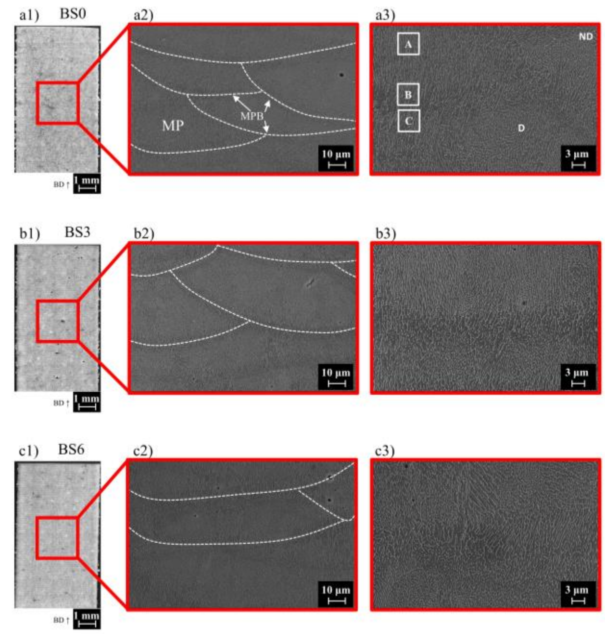

Fig. 6. SEM acquisition showing different magnifications of the microstructure for a1-3) BS0, b1-3) BS3 and c1-3) BS6 (P = 200 W, v = 1000 mm/s). Note the different scale bars. BD: Build Direction; BS: Beam Shape; MP: Melt Pool, MPB: Melt Pool Boundary; D: Directional; ND: Non-Directional. A, B, and C identify fine, coarse, and HAZ regions respectively.

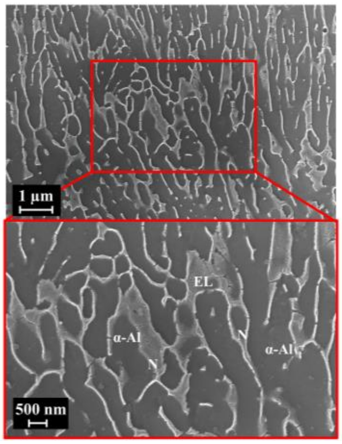

Fig. 7. SEM high magnification images of the cellular/dendritic microstructure for the sample manufactured with BS6, P=200W and v=1000 mm/s. α-Al, EL and N stands for α aluminium matrix, Eutectic Lamellae and Si-rich discontinuous Network, respectively.

Moving towards the centre of the melt pools, grains become columnar and more perpendicular to the melt pool boundaries. Moreover, a small degree of epitaxy can be observed since some grains grew within the melt pool boundaries. These observations are consistent with the work done by Qin et al. [18] dealing with a similar aluminium grade. When using higher BS index, grains become coarser and predominantly columnar, oriented along the melt pool centrelines which coincide with the direction of growth and the heat flow direction. This directional growth differs from that obtained with a Gaussian distribution since columnar grains extend to all the melt pool, not just in the melt pool centrelines, with extensive epitaxy within the melt pool boundaries. Grain coarsening and elongation is accompanied by a reduction of grain boundaries in the direction orthogonal to build direction.

3.4. Crystallographic texture

In Fig. 8 (100), (110) and (111) PF and IPF are shown from the cross section parallel to the build direction. In Fig. 7, Z identifies the direction orthogonal to the build direction and exiting from the metallographic section analyzed. Considering index BS0, the corresponding PFs shows weak <111> texture as well as <110> texture, as shown in the diffraction peak of the IPF from Z direction. Looking at PFs of index BS1-6, the <100> texture can be observed for few grains mostly growing towards the melt pool centerlines (red colored grains from IPF figures). Meanwhile, diffraction peaks from IPFs from Z direction do show relevant contribution of the <111> texture. Increasing the BS index corresponds to a weaker <110> texture. With BS6 the <111> texture becomes dominant (blue colored grains). For the samples produced with BS6 a significative epitaxial grain growth between the melt pool boundaries can be observed. Grains that feature the <111> crystallographic texture can be found either at the centerline and at the borders of the melt pools. Looking at Fig. 8g, diffraction peak in the IPF confirms the PF result.

In the literature, Kotadia et al. [20] pointed out that Al-alloys usually exhibit columnar primary Al grains with <100> crystallographic texture along the build direction when processed with LPBF. Qin et al. [18] also observed the <100> texture development with AlSi10Mg using a Gaussian distribution. The different textures observed throughout this work may be attributable to the convective inert gas flow injected during the process.

The investigations indicate that the beam shape has a direct impact on the microstructural formation. The irradiance distribution is expected to generate a different thermal field on the powder bed changing the melt pool shape. The work confirms that in 3D freestanding samples, beam shape can alter the material properties flexibly in terms of grain structure and crystallographic texture. The programming of beam shapes as a function of melted region in the part can allow the tailoring of mechanical properties in the future. As shown by the crystal structures, material rigidity and plastic deformation capabilities can be manipulated locally achieving gradient material properties.

4. Conclusions

In this work, a systematic investigation on the effect of novel irradiance profile generated by a multi-core fiber laser source on surface roughness and microstructure properties of a well-processable AlSi7Mg0.6 alloy is presented. The results demonstrated that the irradiance characteristics of the beam can play a key-role in the control of microstructure and functional properties of 3D printed parts. The overall results can be summarized as follows:

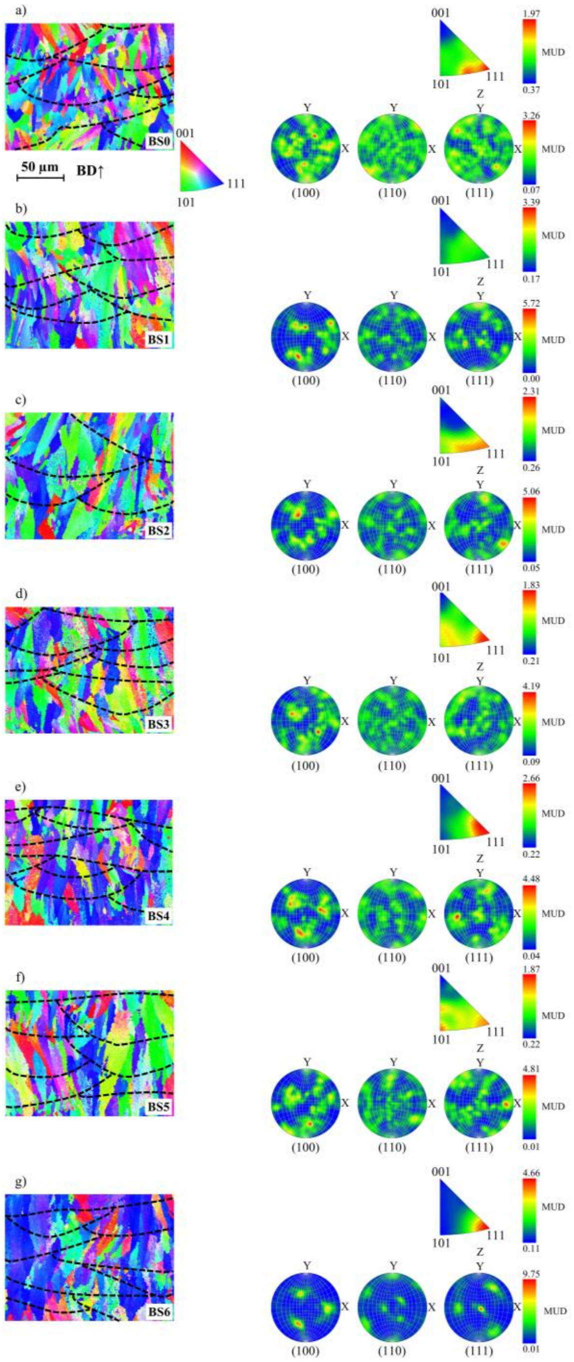

Fig. 8. Orientation maps, grain size distribution, (100) – (110) – (111) pole figures and inverse poles from Z direction for a) BS0, b) BS1, c) BS2, d) BS3, e) BS4, f) BS5, g) BS6. For orientation maps the scale bar is the same and dotted lines indicate the melt pool boundaries. Z direction identifies the orthogonal direction to build direction exiting the cross section.

- Seven different beam profiles from Gaussian to ring-shaped could successfully build freestanding components in LPBF. The use of a non-Gaussian beam shape showed qualitatively a reduction of the sparks and spatter during the process.
- Ring profiles induced a lower areal surface roughness. This result suggests that surface roughness in the upskin and border regions may be optimized with the proper choice of ring

profile. The measurements were supported by observation of spatter generation.

- The observed microstructure is arranged in a cellular-dendritic pattern typical of Al-based hypereutectic alloys, irrespective from the beam shape adopted.
- Stronger epitaxial grain growth is observed at the melt pool boundaries when using a ring profile instead of a Gaussian distribution. Grains appear coarsened, bigger, and elongated along the build direction.
- Despite the grain structure is consistent with the solidification pattern induced from LPBF process, the crystallographic texture of the samples did not show the typical <100> texture typical of cubic materials. No visible trend of texture could be observed as a function of the beam shape.

The results shown in this work allowed to demonstrate how ring-shape beams can influence the microstructure properties, especially in terms of grain structure. Controlling grain structure of LPBF Al-alloys in a reproducible manner is crucial for the manipulation of mechanical properties. Indeed, these family of alloys usually needs extensive heat treatment to address demanding functional requirements. Engineering the light source in terms of beam characteristics offers a potential alternative to design the material properties while exploiting the shape freedom of the LPBF process, without necessarily undergoing post processing heat treatment stages. Moreover, the initial results of surface roughness indicated a potential use of non-Gaussian beam shapes in the optimization of contour strategies for the optimization of surface quality of the as-built parts.

Acknowledgements

The authors acknowledge the support of the Italian Ministry of University and Education (MIUR) through the National Plan of Recovery and Resilience (PNRR). The authors are thankful to nLIGHT Inc. and Optoprim Srl for the laser source used throughout the experimental activity. Raylase GmbH and Direct Machining Control are acknowledged for the technical support and the continuous development of the products used during the project.

References

[1] T. T. Roehling *et al.*, “Controlling grain nucleation and morphology by laser beam shaping in metal additive manufacturing,” *Mater Des*, vol. 195, p. 109071, 2020, doi: 10.1016/j.matdes.2020.109071.

[2] A. Laskin, J. Volpp, V. Laskin, T. Nara, and S. R. Jung, “Multispot optics for beam shaping of high-power single-mode and multimode lasers,” *J Laser Appl*, vol. 33, no. 4, p. 042046, 2021, doi: 10.2351/7.0000461.

[3] T. U. Tumkur *et al.*, “Nondiffractive beam shaping for enhanced optothermal control in metal additive manufacturing,” *Sci Adv*, vol. 7, no. 38, pp. 1–12, 2021, doi: 10.1126/sciadv.abg9358.

[4] R. Shi, S. A. Khairallah, T. T. Roehling, T. W. Heo, J. T. McKeown, and M. J. Matthews, “Microstructural control in metal laser powder bed fusion additive manufacturing using laser beam shaping strategy,” *Acta Mater*, vol. 184, pp. 284–305, 2020, doi: 10.1016/j.actamat.2019.11.053.

[5] M. Liu, K. Wei, X. Yue, G. Huang, J. Deng, and X. Zeng, “High power laser powder bed fusion of AlSi10Mg alloy_ Effect of laser beam mode,” *J Alloys Compd*, vol. 909, p. 164779, 2022, doi: 10.1016/j.jallcom.2022.164779.

[6] T. M. Wischeropp, H. Tarhini, and C. Emmelmann, “Influence of laser beam profile on the selective laser melting process of AlSi10Mg,” *J Laser Appl*, vol. 32, no. 2, p. 022059, 2020, doi: 10.2351/7.0000100.

[7] M. Cloots, P. J. Uggowitzer, and K. Wegener, “Investigations on the microstructure and crack formation of IN738LC samples processed by selective laser melting using Gaussian and doughnut profiles,” *Mater Des*, vol. 89, pp. 770–784, 2016, doi: 10.1016/j.matdes.2015.10.027.

[8] A. Metel, M. Stebulyanin, S. Fedorov, and A. Okunkova, “Power Density Distribution for Laser Additive Manufacturing (SLM): Potential, Fundamentals and Advanced Applications,” *Technologies (Basel)*, vol. 7, no. 1, p. 5, 2018, doi: 10.3390/technologies7010005.

[9] Q. Li, M. Luo, Z. Mu, A. Huang, and S. Pang, “Improving laser welding via decreasing central beam density with a hollow beam,” *J Manuf Process*, vol. 73, pp. 939–947, Jan. 2022, doi: 10.1016/j.jmapro.2021.12.001.

[10] L. Wang, X. Gao, and F. Kong, “Keyhole dynamic status and spatter behavior during welding of stainless steel with adjustable-ring mode laser beam,” *J Manuf Process*, vol. 74, pp. 201–219, Feb. 2022, doi: 10.1016/j.jmapro.2021.12.011.

[11] L. Wang *et al.*, “Adjustable Ring Mode (ARM) laser welding of stainless steels,” *Opt Lasers Eng*, vol. 137, no. August 2020, p. 106360, 2021, doi: 10.1016/j.optlaseng.2020.106360.

[12] J. Grünewald, V. Blickle, M. Allenberg-Rabe, P. Wagenblast, and K. Wudy, “Flexible and highly dynamic beam shaping for Laser-Based Powder Bed Fusion of metals,” *Procedia CIRP*, vol. 111, pp. 65–70, 2022, doi: 10.1016/j.procir.2022.08.124.

[13] J. Grünewald, F. Gehringer, M. Schmöller, and K. Wudy, “Influence of Ring-Shaped Beam Profiles on Process Stability and Productivity in Laser-Based Powder Bed Fusion of AISI 316L,” pp. 1–18, 2021.

[14] F. Galbusera, L. Caprio, B. Previtali, and A. G. Demir, “The influence of novel beam shapes on melt pool shape and mechanical properties of LPBF produced Al-alloy,” *J Manuf Process*, vol. 85, pp. 1024–1036, Jan. 2023, doi: 10.1016/j.jmapro.2022.12.007.

[15] D. A. Kliner *et al.*, “Advanced metal processing enabled by fiber lasers with tunable beam properties,” no. March, p. 18, 2022, doi: 10.1117/12.2614728.

[16] nLIGHT Inc, “AFX User Manual Single-mode Fiber Laser with Programmable Beam Shaping.” 2020.

[17] W. M. Steen and J. Mazumder, *Laser Material Processing*. London: Springer London, 2010. doi: 10.1007/978-1-84996-062-5.

[18] H. Qin, V. Fallah, Q. Dong, M. Brochu, M. R. Daymond, and M. Gallerneault, “Solidification pattern, microstructure and texture development in Laser Powder Bed Fusion (LPBF) of Al10SiMg alloy,” *Mater Charact*, vol. 145, no. August, pp. 29–38, 2018, doi: 10.1016/j.matchar.2018.08.025.

[19] F. Galbusera, L. Caprio, B. Previtali, and A. G. Demir, “The influence of novel beam shapes on melt pool shape and mechanical properties of LPBF produced Al-alloy,” *J Manuf Process*, vol. 85, pp. 1024–1036, Jan. 2023, doi: 10.1016/j.jmapro.2022.12.007.

[20] H. R. Kotadia, G. Gibbons, A. Das, and P. D. Howes, “A review of Laser Powder Bed Fusion Additive Manufacturing of aluminium alloys: Microstructure and properties,” *Addit Manuf*, vol. 46, no. June, p. 102155, 2021, doi: 10.1016/j.addma.2021.102155.